Quantum Science and Technology

PAPER

# Einstein–Podolsky–Rosen paradox with position–momentum entangled macroscopic twin beams

RECEIVED
6 February 2021

REVISED
8 June 2021

ACCEPTED FOR PUBLICATION
6 August 2021

PUBLISHED
25 August 2021

**Ashok Kumar**[1,2], **Gaurav Nirala**[1,3] **and Alberto M Marino**[1,3,*]

[1] Homer L Dodge Department of Physics and Astronomy, The University of Oklahoma, Norman, OK 73019, United States of America
[2] Department of Physics, Indian Institute of Space Science and Technology, Thiruvananthapuram, Kerala 695547, India
[3] Center for Quantum Research and Technology, The University of Oklahoma, Norman, OK 73019, United States of America
[*] Author to whom any correspondence should be addressed.

**E-mail:** marino@ou.edu

**Keywords:** Einstein–Podolsky–Rosen paradox, bright entangled twin beams, spatial entanglement, spatial squeezing

## Abstract

Spatial entanglement is at the heart of quantum enhanced imaging applications and high-dimensional quantum information protocols. In particular, for imaging and sensing applications, quantum states with a macroscopic number of photons are needed to provide a real advantage over the classical state-of-the-art. We demonstrate the Einstein–Podolsky–Rosen (EPR) paradox in its original position and momentum form with bright twin beams of light by showing the presence of EPR spatial (position–momentum) entanglement. An electron-multiplying charge-coupled-device camera is used to record images of the bright twin beams in the near and far field regimes to achieve an apparent violation of the uncertainty principle by more than an order of magnitude, which remains statistically significant even in the limit of a small number of images. We further show that the presence of quantum correlations in the spatial and temporal degrees of freedom leads to spatial squeezing of the bright twin beams in both the near and far fields. This provides another verification of the spatial entanglement and points to the presence of hyperentanglement in the bright twin beams.

## 1. Introduction

Over the last several decades, quantum entanglement has been studied extensively and is now considered to be an indispensable resource for the emerging field of quantum technologies [1–12]. Spatial entanglement, in particular, has attracted significant attention for applications in quantum information science as it exists in an infinite dimensional Hilbert space [13–21]. The increased dimensionality of the spatial degree of freedom can enable, for example, an exponential speed-up for quantum computation, enhanced quantum channel capacities, and security enhancements of quantum communication protocols [22–27]. Furthermore, spatial quantum correlations can extend quantum enhancements from the time domain to the spatial one to enable quantum imaging and quantum metrology with enhanced sensitivity and resolution [28–35].

Spatial quantum correlations were central to the original Einstein–Podolsky–Rosen (EPR) paper of 1935 [36] that questioned the completeness of quantum mechanics. The EPR paper considered a *gedanken* experiment involving a pair of entangled particles with a space-like separation. The presence of perfect correlations between their positions and momenta led to an apparent violation of Heisenberg's uncertainty principle. Such an apparent violation is now known as the EPR paradox and it arises from imposing local realism on a pair of distant quantum correlated particles treated as two independent systems [4, 37–40].

Experiments similar to the EPR thought experiment have now been performed with correlated photon pairs produced with parametric down conversion [13–16] and with ultracold atomic ensembles [41–43]. For the optical regime, initial experiments were performed in the time domain through the use of slits to select different spatial regions and temporal coincidence measurements with avalanche photodiodes [13]. More direct measurements of the spatial (position–momentum) quantum correlations were later

performed with an electron-multiplying charge-coupled-device (EMCCD) camera [14–16]. EPR entanglement was demonstrated by a verification of the EPR paradox through the violation of an inequality equivalent to Heisenberg's uncertainty principle [44, 45].

While previous experiments [13–16] have provided significant insight into the nature of spatial quantum correlations, they have limited applicability for applications such as quantum sensing and imaging. This is due to the long integration times and/or large number of images required to observe quantum effects. The ability to generate and measure macroscopic quantum states that exhibit EPR spatial entanglement would make it possible to overcome such limitations. To this extent, *in vivo* imaging of dynamic biological samples with low damage thresholds [46] and imaging of atomic systems such as Bose–Einstein condensates [47, 48] and trapped single atoms [49] provide ideal applications for macroscopic quantum states with spatial quantum correlations, as imaging over extended periods of time is not an option. In addition, such macroscopic quantum states would boost the sensitivity of a given measurement due to the scaling of the signal-to-noise ratio with the number of photons. In practice, to surpass the classical state-of-the-art and make a difference for real-life applications, quantum states need to have a power close to the threshold limit of the system to be enhanced. Once this limit is reached, further enhancements can only be obtained with quantum resources. From a fundamental perspective, given the role that entanglement plays in quantum information science and quantum technology, it is important to understand the impact of scaling from a few to a large number of photons on entanglement and quantum properties in different degrees of freedom.

Here we demonstrate the EPR paradox in its original position–momentum form with macroscopic entangled beams of light, or bright twin beams, through measurements with an EMCCD. The photon flux of the bright twin beams is $\sim 10^{14}$ photons per second per beam and is limited by the saturation of the EMCCD. We show the presence of EPR position–momentum entanglement in the bright twin beams through a violation of the EPR criterion by more than an order of magnitude and demonstrate that a statistically significant violation is possible even with less than 10 images. Moreover, we show that an interplay between quantum correlations in different degrees of freedom, spatial and temporal, leads to sub-shot noise spatial noise statistics, i.e. spatial squeezing. The presence of spatial squeezing in both the near and far fields provides an additional verification of spatial entanglement in the twin beams through an inequality analogous to the Duan criterion [50].

To demonstrate the EPR paradox, the measured relative uncertainties in position and momentum between the twin beams must show an apparent violation of Heisenberg's uncertainty. This can be quantified through a violation of the EPR criterion, which is given by

$$\Delta^2(r_2|r_1)\,\Delta^2(p_2|p_1) \geqslant \hbar^2/4, \tag{1}$$

where $\Delta^2(r_2|r_1)$ ($\Delta^2(p_2|p_1)$) represents the variance in measuring position $r_2$ (momentum $p_2$) of one of the photons conditioned on the measurement of position $r_1$ (momentum $p_1$) of the other photon. Direct characterization of $\Delta^2(r_2|r_1)$ and $\Delta^2(p_2|p_1)$ is possible via spatial cross-correlation measurements between captured images of the twin beams in the near and far field regimes, respectively. For brevity and simplicity of notation, throughout the rest of the manuscript we use the notation $\Delta^2 r \equiv \Delta^2(r_2|r_1)$ and $\Delta^2 p \equiv \Delta^2(p_2|p_1)$, such that $\Delta r = \sqrt{\Delta^2(r_2|r_1)}$ and $\Delta p = \sqrt{\Delta^2(p_2|p_1)}$ represent the position and momentum conditional uncertainties, respectively.

## 2. Experiment

To measure the near and far field properties of the twin beams, we use the experimental setups shown in figures 1(a) and (b), respectively. In both setups the positions of the source (Rb vapor cell) and EMCCD are kept fixed while different optical systems are used for each configurations. For the near field we image the cell center to the EMCCD with a 400 mm lenses in a configuration with a demagnification of 0.65. For the far field a 500 mm lens in an *f*-to-*f* configuration generates the Fourier transform of the cell center on the EMCCD. The *f*-to-*f* optical system maps the transverse momenta of the field at the cell center to transverse position on the EMCCD, such that a photon with transverse momentum $\hbar k_\perp$ is mapped to transverse position $x = fk_\perp/k$ in the far field, where $k$ is the magnitude of the total $k$-vector [13]. For both configurations independent optical systems are used for the probe and conjugate beams. The insets to the right of each configuration show the expected correlations between the EMCCD pixels of the acquired probe and conjugate images. Due to the phase matching condition and the fact that the probe and conjugate photons are generated at the same spatial location in the source, in the near field (position correlations) a single pixel (position) in the conjugate will be correlated with a small region (determined by $\Delta r$) centered around the corresponding pixel in the probe. On the other hand, for the far field (momentum

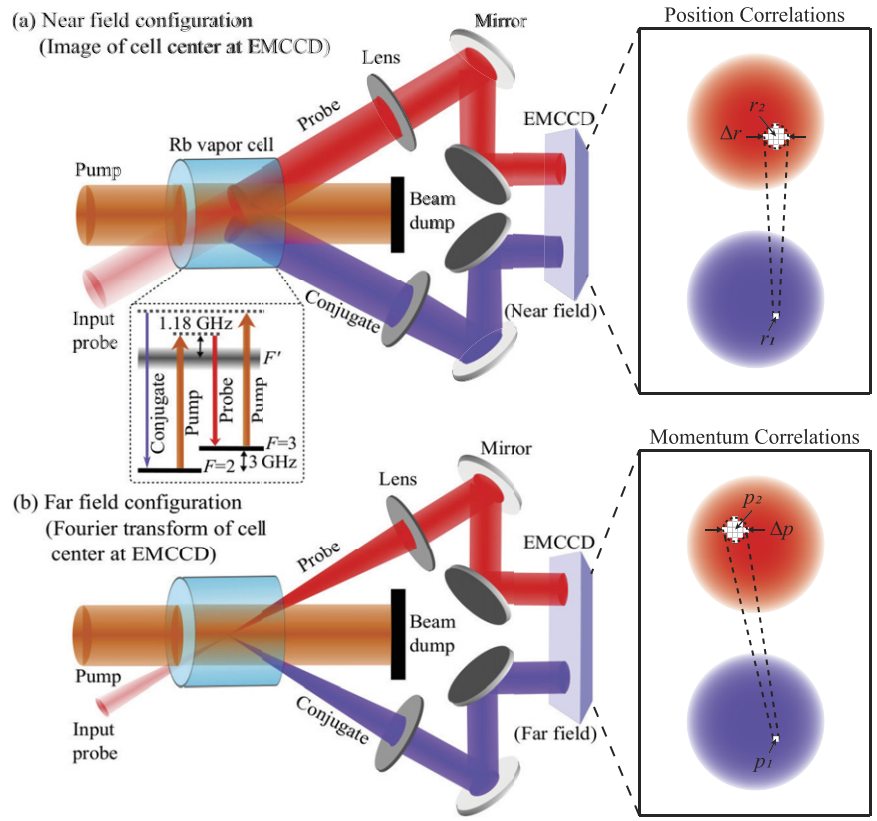


**Figure 1.** Experimental setup to measure (a) position and (b) momentum correlations. For the position correlation measurements (near field) a single lens images the cell center onto the EMCCD, while for the momentum correlation measurements (far field) a single lens in an *f*-to-*f* configuration generates the Fourier transform of the cell center at the EMCCD. The insets to right of each configuration give a graphical representation of the position and momentum correlations between the EMCCD pixels of the measured probe and conjugate images. The inset below the Rb vapor cell shows the double-Λ energy level configuration in the D1 line of $^{85}$Rb used for the four-wave mixing (FWM) process.

correlations), a single pixel (momentum) in the conjugate will be correlated with a small region (determined by $\Delta p$) centered around a pixel that is a reflection around the center (180° rotation) of the probe.

We generate narrowband bright twin beams with a four-wave mixing (FWM) process in a double-Λ configuration in the D1 line of $^{85}$Rb, see inset below the vapor cell in figure 1(a). We use a Ti:Sapphire laser at 795 nm to generate the strong pump beam required for the FWM. An acousto-optic modulator is used to red-shift a portion of the laser by ∼3 GHz to generate the input probe. Pump and probe are then made to intersect at an angle of 0.4 degrees inside a 12 mm long hot $^{85}$Rb vapor cell (temperature of 106°C). In this configuration, two pump photons are absorbed and two new quantum correlated twin photons called probe and conjugate are generated. When seeded, the FWM amplifies the input probe beam and generates a bright conjugate beam to produce bright twin beams. By changing the number of photons in the input seed probe, it is thus possible to obtain a controllable number of quantum correlated photons. This makes it possible to overcome some of the problems that limit the squeezing and number of photons in bright squeezed vacuum states [51, 52].

As previously demonstrated for parametric down conversion, the properties of the spatial quantum correlation of the generated entangled photons are governed by the angular spectrum of the pump and the phase matching condition [33]. The same is true for the FWM process, which means that the spatial entanglement properties of the generated bright twin beams are not determined or modified by the seed (input probe) beam. Note that this is similar to experiments in the time domain, for which the seed beam for the FWM does not affect the quadrature entanglement properties of the source and the generated bright beams effectively act as local oscillators when performing intensity measurements. In our experiments, the role of the seed beam is to stimulate the generation of a macroscopic number of photons in a large number of spatial modes supported by the FWM process. This is necessary given that to observe the spatial correlations a large number of coherence areas (correlation regions shown in figure 1) or spatial modes need to be detected [53] with the EMCCD. As a result, for the near (far) field configuration it is necessary for the probe diameter to be as large (small) as possible at the cell to excite as many spatial regions (*k*-vectors) as possible. This is analogous to the use of a local oscillator that overlaps with a large number of

coherence areas when performing homodyne measurements to characterize the spatial properties [9]. As a result, the input probe beam diameter at the cell center is set to 2.0 mm and 0.4 mm for the near and far field configurations, respectively, while the pump beam diameter is kept fixed at 4.4 mm for both configurations.

## 3. Image acquisition and data analysis

As opposed to experiments done in the single photon regime that are based on coincidence detection, for bright optical fields, as the ones we consider here, the quantum properties need to be characterized through cross-correlation measurements of their fluctuations. This is analogous to measurements done in the time domain for bright quantum states of light. Thus, to characterize the spatial quantum correlation properties of the bright twin beams we first need to obtain the spatial intensity fluctuations of the beams. To do so, for each beam we subtract two images acquired in rapid succession with the kinetic mode feature of the EMCCD camera, which makes it possible to store the detected charge in the CCD sensor itself to allow a burst sequence of images to be acquired. To implement the kinetic mode, we divide the total active sensor area, which consists of 512 × 512 pixels and an additional 512 × 512 pixels buffer region for storage, into a total of six frames, each of size 170 × 512 pixels. When the EMCCD is set to image acquisition, only the topmost frame is exposed to light. After acquiring the top frame, the charge is serially transferred to the next frame below at a speed of 300 ns per row. This process is repeated a total of 6 times and makes it possible to have a time difference of 51 $\mu$s between two adjacent frames. Once all six frames have been acquired, the information, which consists of six frames each with images of the probe and conjugate, is read out of the EMCCD.

During the acquisition of the images of the bright probe and conjugate beams, we pulse the input probe and pump beams with a duration of 1 $\mu$s and 10 $\mu$s, respectively. The timing sequence for the pump and probe pulses in two consecutive frames of the EMCCD camera is shown in figure 2(a). The probe pulse is delayed by 6 $\mu$s with respect to the pump pulse to avoid transients effects in the FWM. To provide enough time for a single pump-probe pulse sequence in a given frame, the camera exposure time per frame is set to 12 $\mu$s. This leads to a time interval between two consecutive images of $\sim$ 60 $\mu$s. Given that this time is longer than the inverse of the bandwidth ($\sim$ 20 MHz) of the FWM process, there are no quantum correlations between images in two consecutive frames. As can be seen in figure 2(b), which shows probe and conjugate images acquired in two consecutive frames, the peak region of the probe (conjugate) image has $\sim 5 \times 10^4$ ($\sim 3.5 \times 10^4$) photocounts per pixel. To obtain images of the spatial intensity fluctuation of each beam, we subtract two probe (conjugate) images acquired in consecutive frames, with the result shown in figure 2(c). As can be seen, the typical scale of the noise intensity fluctuations in both beams is the same. This approach of subtracting images in two consecutive frames also helps to minimize the spatial and temporal classical excess noise introduced by the seeding beam.

The acquisition of the probe and conjugate images with the EMCCD camera is synchronized with the pump–probe pulse timing sequence. We acquire 200 images, each with six frames, of the twin beams in both the near and far field configurations to observe the EPR paradox in position–momentum. We also acquire background images without an input probe beam after every probe-conjugate image acquisition to subtract the background noise due to electronic noise and scattered pump photons as done in reference [54].

To calculate the spatial cross-correlations in the near and far fields, we crop a region of 120 × 120 pixels (80 × 80 pixels) in the spatial intensity fluctuation image of the probe (conjugate) centered around the pixel that corresponds to the intensity maxima of the probe (conjugate). We then scan the cropped region of the conjugate spatial intensity fluctuation image over the cropped probe spatial intensity fluctuation image to evaluate the spatial cross-correlation, given by

$$\mathrm{Corr}(i,j) = \frac{\sum_m \sum_n P_{mn} C_{(m-i)(n-j)}}{\sqrt{\left(\sum_m \sum_n P_{mn}^2\right)\left(\sum_m \sum_n C_{mn}^2\right)}}, \tag{2}$$

where $P_{mn}$ and $C_{mn}$ are the cropped probe and conjugate spatial intensity fluctuation images (represented as matrices), respectively. The summation is done over all elements of the matrices. Note that this approach is equivalent to taking a single pixel of the image of the spatial intensity fluctuations of the conjugate and scanning it over the pixels of the image of the spatial intensity fluctuations of the probe to obtain the correlation or coherence area (shown in the insets to the right in figure 1), repeating with all pixels from the cropped image of the spatial intensity fluctuations of the conjugate, and then averaging over all the calculated coherence areas.

In performing this analysis, for the far field regime we rotate the conjugate spatial intensity fluctuation image by 180° before calculating the cross-correlation. This is due to the transverse momentum

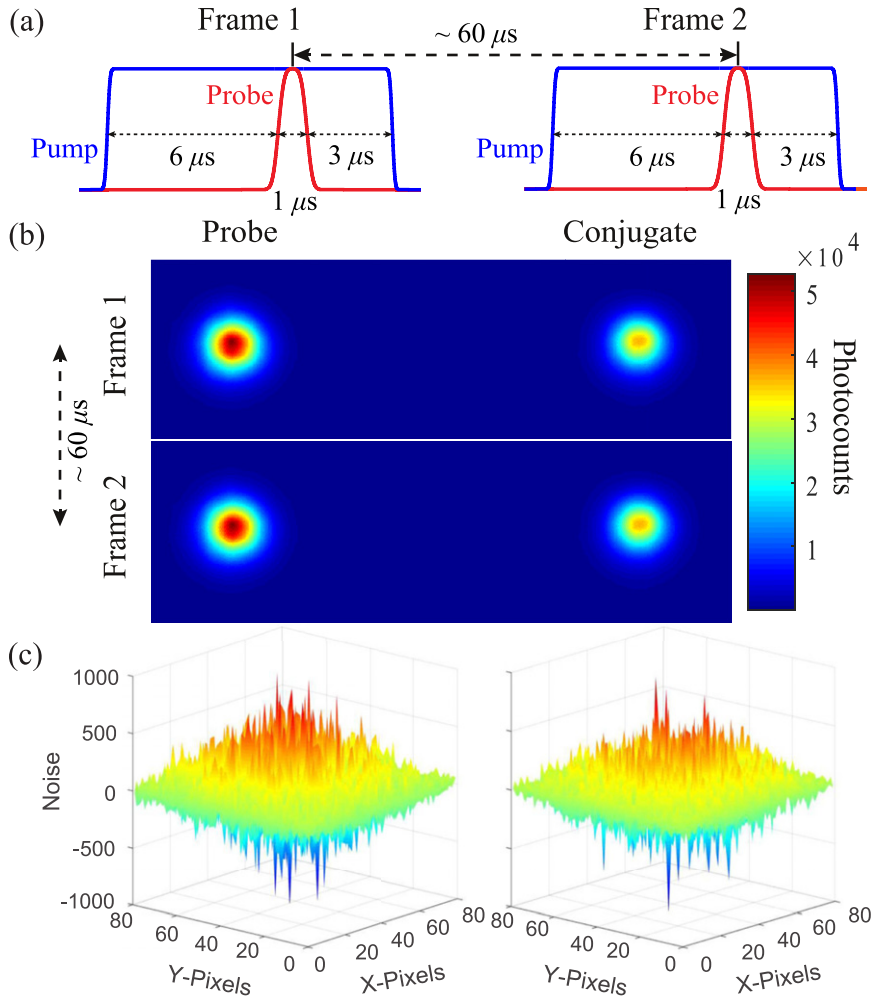


**Figure 2.** (a) Timing sequence for the pump and probe pulses. The temporal separation between two probe pulses, which is synchronized with the acquisition of two consecutive frames of the EMCCD, is ~60 $\mu$s. (b) Images of probe and conjugate pulses acquired in two consecutive frames. (c) Spatial intensity fluctuation images for the probe (left) and conjugate (right) beams obtained after the subtraction of two consecutive frames of the EMCCD. Figure adapted from [18].

anti-correlations that result from the phase matching condition, which in turn make the correlated regions between the probe and conjugate be diametrically opposite to each other in the far field, as schematically shown in figure 1. This is not the case for the near field, as in this case probe and conjugate photons are generated in the same spatial location.

## 4. Results and discussion

The calculated spatial cross-correlations in the near and far field regimes are shown in figure 3. The presence of a peak shows the correlated region, i.e. the coherence area [55], between the probe and conjugate spatial intensity fluctuations. These cross-correlations are proportional to the conditional probability density functions $P(r_2|r_1)$ and $P(p_2|p_1)$ for the near (position) and far (momentum) fields, respectively. Their widths (as characterized by the standard deviation) provide a measure of the conditional uncertainties, $\Delta r$ and $\Delta p$, in obtaining the position ($r_2$) and momentum ($p_2$) of a photon conditioned on the position ($r_1$) and momentum ($p_1$) of the other photon being measured, respectively. As a check, we also performed the cross-correlation measurements with images of coherent state pulses both in the near and far field and, as expected, a correlation peak is not present.

To estimate the conditional uncertainties in position ($\Delta r$) and momentum ($\Delta p$), we fit the cross-correlations shown in figure 3 with a two-dimensional Gaussian function of the form $A\,\mathrm{e}^{-[(x-x_0)^2/2\sigma_x^2+(y-y_0)^2/2\sigma_y^2]}$, where $A$ is a constant and $\sigma_x$ ($\sigma_y$) is the standard deviation along the $x$ ($y$) direction. From the measured cross-correlations we obtain $\sigma_x = 4.27 \pm 0.10$ pixels and $\sigma_y = 3.52 \pm 0.08$ pixels in the near field, and $\sigma_x = 4.78 \pm 0.13$ pixels and $\sigma_y = 4.90 \pm 0.13$ pixels in the far field, where the uncertainties represent the 95% confidence intervals of the fits. To translate these standard deviations in

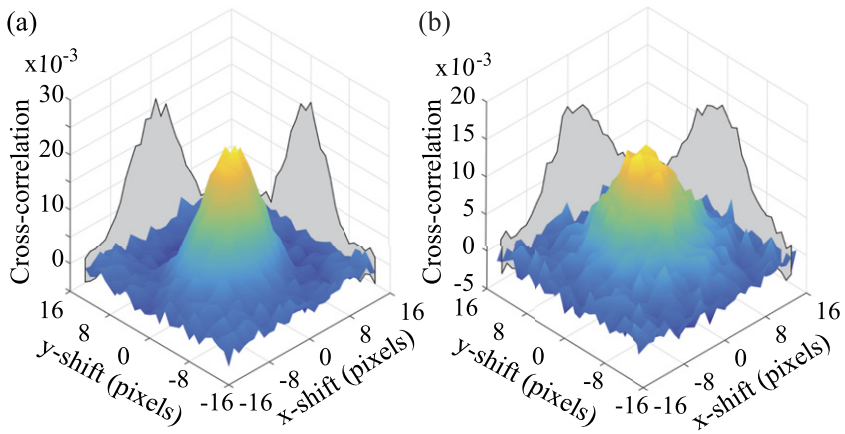


**Figure 3.** Spatial cross-correlations between the intensity fluctuations of the probe and conjugate measured in the (a) near and (b) far field configurations.

pixels from the EMCCD plane to real position and momentum conditional uncertainties at the source (Rb vapor cell), we take into account the transformations performed by the optical systems used to acquire the images. For the near field measurements, we take into account the demagnification factor $M = 0.65$ of the imaging system to translate to actual position, such that $\Delta r_i = \sigma_i s/M$, where $i = \{x, y\}$ and $s = 16$ $\mu$m is the linear pixel size. Similarly, for the far field measurements we take into account the transformation performed by the $f$-to-$f$ optical system to translate to actual momentum, such that $\Delta p_i = \frac{2\pi\hbar}{\lambda f}\sigma_i s$, where $i = \{x, y\}$, $\lambda$ is the wavelength of the light (795 nm), and $f$ is the focal length of the Fourier lens (500 mm).

After performing the necessary transformations, we obtain the products defined in equation (1) along the $x$ and $y$ directions

$$\Delta^2 r_x \, \Delta^2 p_x = (1.62 \pm 0.12) \times 10^{-2}\hbar^2 < \hbar^2/4, \tag{3}$$

$$\Delta^2 r_y \, \Delta^2 p_y = (1.15 \pm 0.08) \times 10^{-2}\hbar^2 < \hbar^2/4. \tag{4}$$

These results represent a violation of the EPR criterion by more than one order of magnitude, thus verifying the EPR paradox with quantum states of light containing a macroscopic number of photons. To determine the number of images needed for the violation of the EPR criterion to be statistically significant, we define the confidence level parameter ($C$) along the lines of reference [56]

$$C_i = \left| \frac{1/4 - \Delta^2 r_i \, \Delta^2 p_i}{\delta} \right|, \tag{5}$$

where $i = \{x, y\}$ and $\delta$ is the standard deviation in the estimation of the product $\Delta^2 r_i \Delta^2 p_i$. We consider the violation to be statistically significant when $C > 5$, which represents a violation by more than 5 standard deviations.

We calculate the spatial cross-correlations in the near and far fields for different number $N$ of images and obtain the product $\Delta^2 r_i \Delta^2 p_i$ for each set of images. To obtain $\delta$, we take the 68% confidence intervals from the fits and use error propagation to obtain the standard deviation in the estimation of this product. We repeat this procedure as many times as possible given the number of images $N$ used for the analysis and the available 200 images. That is, for $N = 5$ we obtain 40 different values of $C$, for $N = 10$ we obtain 20 different values, and so on. Finally, for each value of $N$ we average over all the values of $C$ to obtain a more accurate estimation of this parameter.

Figure 4(a) shows the confidence level ($C$) as a function of the number of images ($N$) used for the analysis. The blue squares and green circles representing the calculated values of $C$ along the $x$ and $y$ directions, respectively. The dashed lines give a fit of the calculated values of $C$ to the function $A_0\sqrt{N}$, where $A_0$ is a fit parameter. As expected, $C$ increases as $N$ increases and scales as $\sqrt{N}$. As can be seen, we get a statistically significant violation of the EPR criterion even when we perform the analysis with five images. Although, for such a small number of images the fit of the cross-correlation functions to the Gaussian function is not as good due to the low signal-to-noise ratio. This results in a slight increase in the product $\Delta^2 r_i \Delta^2 p_i$ shown in figure 4(b) for $N = 5$. However, we can safely claim that a statistically significant violation of the EPR criterion is obtained for $N < 10$. It is important to note that from the scaling of $C$ with $N$, as shown by the fits in figure 4(a), in principle a statistically significant violation with $C > 25$ is possible

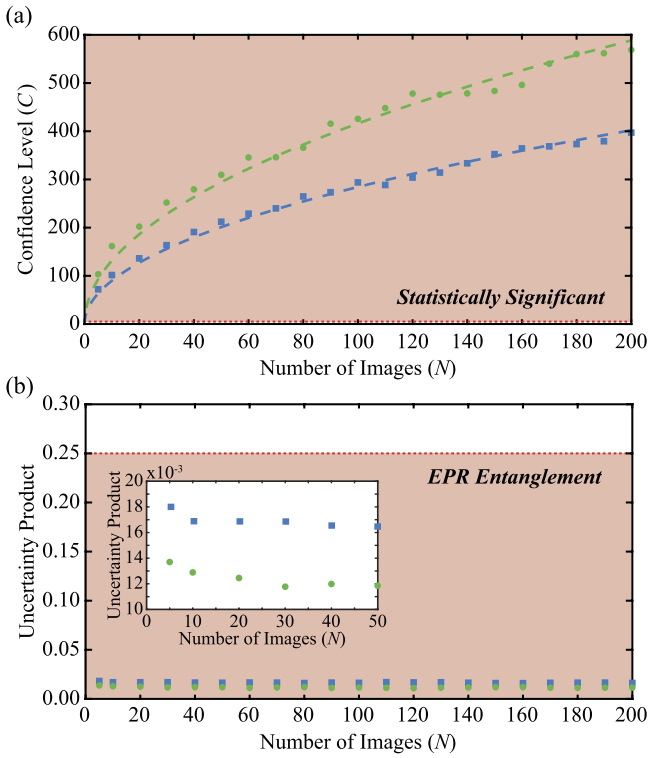


**Figure 4.** (a) Confidence level $C$ as a function of the number of images $N$ used for the analysis. The blue squares and green circles represent the calculated values of $C$ along the $x$ and $y$ directions, respectively, while the dashed lines correspond to a fit of the form $A_0\sqrt{N}$ with fit parameter $A_0$. The region above the dotted red line (shaded in red) corresponds to $C > 5$, which represents a statistically significant violation of the EPR criterion. (b) Product $\Delta^2 r_i \Delta^2 p_i$ as a function of the number of images $N$ used for the analysis. The region below the dotted red line (shaded in red) indicates a violation of the EPR criterion and thus the presence of EPR entanglement. The inset shows a zoom in for the region $N < 50$. Measurements along the $x$ and $y$ directions are shown with blue squares and green circles, respectively.

even with a single image. This is in stark contrast to the $\sim 10^4$–$10^5$ images [14, 16, 56] or about three orders of magnitude longer integration times [57] required for photon pair experiments.

An alternative way to verify the quantum nature of the spatial correlations is through the inseparability criterion, which is based on the total noise properties of two non-commuting observables [50]. For position and momentum, this criterion states that the system is entangled if the inseparability parameter $I$ satisfies the relation

$$I = \langle \Delta^2 \hat{R} \rangle + \langle \Delta^2 \hat{P} \rangle < 2, \tag{6}$$

where $\langle \Delta^2 \hat{R} \rangle = \langle \Delta^2 (\hat{r}_\mathrm{p} - \hat{r}_\mathrm{c}) \rangle$ and $\langle \Delta^2 \hat{P} \rangle = \langle \Delta^2 (\hat{p}_\mathrm{p} + \hat{p}_\mathrm{c}) \rangle$ are position difference and momentum sum variances, respectively, normalized to their corresponding shot noise. Thus, the presence of spatial squeezing between the probe and conjugate in both the near and far fields indicates that there is spatial entanglement between them.

To show the sub-shot noise behavior, we start with 120 × 120 pixel cropped regions of the probe and conjugate images centered around the corresponding intensity maximum and align them with an image registration algorithm [54]. After the alignment, we crop a region of 80 × 80 pixels of each probe and conjugate image around its center for the final noise analysis. We characterize the spatial quantum noise ratio (NR) with the ratio

$$\mathrm{NR} \equiv \frac{\langle \Delta^2 [(N_{\mathrm{p}1} - N_{\mathrm{p}2}) - (N_{\mathrm{c}1} - N_{\mathrm{c}2})] \rangle}{\langle N_{\mathrm{p}1} + N_{\mathrm{c}1} + N_{\mathrm{p}2} + N_{\mathrm{c}2} \rangle}, \tag{7}$$

where $(N_{\mathrm{p}1}, N_{\mathrm{c}1})$ and $(N_{\mathrm{p}2}, N_{\mathrm{c}2})$ are the matrices representing the photo-counts per pixel for the cropped regions in the probe and conjugate images for the two consecutive frames used for the analysis, respectively. The statistics are calculated over the spatial photo-counts registered by the pixels of the EMCCD. Thus, the numerator represents the relative spatial variance between the probe and conjugate spatial intensity fluctuations, while the denominator represents the shot noise limit (SNL). Therefore NR = 1 corresponds to a coherent state and NR < 1 to a spatially squeezed state. When this analysis is performed in the near (far) field configuration NR corresponds to $\langle \Delta^2 \hat{R} \rangle$ ($\langle \Delta^2 \hat{P} \rangle$).

Given that the correlated regions are spread over more than one pixel, as shown in figure 3 and schematically in figure 1, an accurate measure of NR is obtained only when the noise analysis is performed

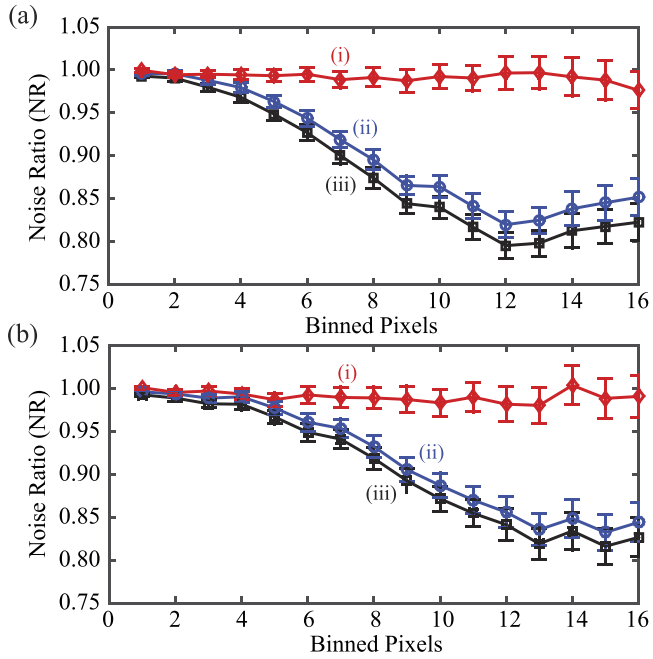


**Figure 5.** Measured NR as a function of binning in the (a) near and (b) far fields. The number of binned pixels given along the $x$ axes represent the number of pixels used along each side of a square binning region. Traces (i), (ii), and (iii) represent the SNL, squeezing without background noise subtraction, and squeezing with background subtraction, respectively. Error bars represent the standard deviation of the mean for the NR over the 200 acquired images.

after grouping or binning a square pixel region into 'super-pixels' larger than the coherence area [18, 53, 54]. Figures 5(a) and (b) show NR as a function of binning in the near and far fields, respectively. For both figures, trace (i) shows the SNL, while traces (ii) and (iii) represent the NRs for the twin beams without and with background correction, respectively. The SNL is measured by splitting the probe laser into two beams of equal power and performing the same noise analysis as with the bright twin beams. During these measurements the pump is turned off so that there is no FWM process or scattered pump background noise. As expected, NR $= 1$ for the measured SNL in both the near and far field configurations. The minimum NRs in the near and far field configurations are $0.84 \pm 0.02$ and $0.83 \pm 0.02$, respectively, without background noise subtraction and $0.82 \pm 0.02$ and $0.81 \pm 0.02$, respectively, with background subtraction. This translates to an inseparability parameter, $I$, of $1.67 \pm 0.03$ without background noise subtraction and $1.63 \pm 0.03$ with background noise subtraction, which shows that the generated bright twin beams contain spatial entanglement.

Even though the criterion to demonstrate EPR entanglement is more stringent than the one for inseparability, we see a significantly larger violation of the EPR criterion than a reduction of the inseparability parameter. The reason for this is that the measurements performed to verify the EPR paradox are purely spatial in nature and as such directly quantify the spatial quantum properties of the system. On the other hand, as shown in appendix A, the measurements to show the inseparability criterion result from an interplay between quantum correlations in the spatial and temporal domains. More specifically, the measured level of spatial squeezing is limited by the degree of amplitude quadrature squeezing present in the twin beams. While this means that the inseparability criterion does not provide a pure measure of the degree of spatial entanglement, it does point to the presence of quantum correlations in multiple degrees of freedom (spatial and temporal) in the twin beams. This result, combined with previous measurements with the FWM source that show the presence of quadrature entanglement in this system [9, 10], provides a good indication of the presence of hyperentanglement in the FWM generated bright twin beams.

## 5. Conclusion

In conclusion, we have demonstrated the EPR paradox in its original position–momentum form with macroscopic quantum states of light. The use of bright twin beams has made it possible for us to show a statistically significant violation of the EPR criterion with less than 10 images. We have further verified the presence of spatial entanglement through the inseparability criterion by measuring spatial squeezing in both the near and far fields. As we show, the presence of spatial squeezing results from an interplay between

quantum correlations in the spatial and temporal degrees of freedom. Thus, the results presented point to the presence of hyperentanglement in the generated bright twin beams. The ability to generate spatially entangled bright twin beams makes the FWM system a unique choice to enable quantum enhanced sensing and quantum imaging configurations that can surpass the classical state-of-the-art. Moreover, the narrowband bright twin beams generated with the FWM process are ideal candidates for quantum information processing based on atomic ensembles [58]. The results presented thus provide a path for many novel quantum technologies to move out of the laboratory and into real-life applications.

## Acknowledgments

This work was supported by the National Science Foundation (NSF) (Grant No. PHYS-1752938) and by the W M Keck Foundation.

## Appendix A. Relation between spatial and temporal squeezing

We present detailed calculations that show the relationship between squeezing in the temporal and spatial domains. As outlined in the main text, we characterize the spatial squeezing through the noise reduction factor (NR) defined as the ratio of the spatial variance of the difference between the fluctuations of the probe and conjugate to the corresponding shot noise. We can then write NR in terms of number operators as

$$\mathrm{NR} \equiv \frac{\langle \Delta^2[(\hat{N}_{\mathrm{p1}} - \hat{N}_{\mathrm{p2}}) - (\hat{N}_{\mathrm{c1}} - \hat{N}_{\mathrm{c2}})]\rangle}{\langle \Delta^2[(\hat{N}_{\mathrm{p1}} - \hat{N}_{\mathrm{p2}}) - (\hat{N}_{\mathrm{c1}} - \hat{N}_{\mathrm{c2}})]\rangle_{\mathrm{CS}}}, \tag{A.1}$$

where $\hat{N}_{\mathrm{p}i}$ and $\hat{N}_{\mathrm{c}i}$ are the number operators for the probe and conjugate images, respectively, acquired in frame $i = \{1, 2\}$. In this equation the subscript CS indicates that the variance is to be evaluated for coherent states equivalent to the probe and conjugate beams. Note that for a coherent state the variance is equal to its mean, such that equation (A.1) takes the form given in equation (7) of the main text. To relate this expression to the degree of temporal squeezing, we first consider the operator for the number of photons measured by the EMCCD for a given image, that is

$$\hat{N} = \int_A \mathrm{d}\vec{x} \int_{t_{\mathrm{d}}} \mathrm{d}t\, \hat{n}(\vec{x}, t), \tag{A.2}$$

where the spatial integral is over the analysis region $A$ of the images captured by the EMCCD, the temporal integral is over the detection time $t_{\mathrm{d}}$, and $\hat{n}(\vec{x}, t)$ is the spatially dependent photon flux of the beam incident on the EMCCD. In order to study the spatial properties of the light, we need to take into account the fact that the EMCCD is composed of pixels, which allows us to write

$$\hat{N} = \sum_{i,j} \int_{D_{ij}} \mathrm{d}\vec{x} \int_{t_{\mathrm{d}}} \mathrm{d}t\, \hat{n}(\vec{x}, t) = \sum_{i,j} \int_{D_{ij}} \mathrm{d}\vec{x} \int_{t_{\mathrm{d}}} \mathrm{d}t\, [\langle \hat{n}(\vec{x}, t)\rangle + \delta\hat{n}(\vec{x}, t)], \tag{A.3}$$

where $D_{ij}$ is the area of pixel $(i, j)$ and the summation is over all the EMCCD pixels in the analysis region $A$. For the last equality we have expressed the spatially dependent flux $\hat{n}(\vec{x}, t)$ as a sum of the contributions from its mean value $\langle \hat{n}(\vec{x}, t)\rangle$ and its fluctuations $\delta\hat{n}(\vec{x}, t)$, with $\langle \delta\hat{n}(\vec{x}, t)\rangle = 0$.

Next, we consider the subtraction of two subsequent frames taken a time $\Delta t$ apart

$$\delta\hat{N} = \hat{N}_1 - \hat{N}_2 = \sum_{i,j} \int_{D_{ij}} \mathrm{d}\vec{x} \int_{t_{\mathrm{d}}} \mathrm{d}t\, [\langle \hat{n}_1(\vec{x}, t)\rangle - \langle \hat{n}_2(\vec{x}, t + \Delta t)\rangle + \delta\hat{n}_1(\vec{x}, t) - \delta\hat{n}_2(\vec{x}, t + \Delta t)]. \tag{A.4}$$

Here, we consider the case in which $\Delta t$ is short enough such that the spatially dependent mean value does not change from one frame to the other, but significantly longer than the inverse of the bandwidth of the process such that the quantum properties are uncorrelated both in space and time. In this case we have that

$$\begin{aligned} \langle \hat{n}_1(\vec{x}, t)\rangle &= \langle \hat{n}_2(\vec{x}, t + \Delta t)\rangle, \\ \langle \delta\hat{n}_1(\vec{x}, t)\delta\hat{n}_2(\vec{x}', t + \Delta t)\rangle &= 0, \end{aligned} \tag{A.5}$$

where we are assuming the ideal case of no technical noise. Thus, equation (A.4) simplifies to

$$\delta\hat{N} = \sum_{i,j}\int_{D_{ij}} \mathrm{d}\vec{x}\int_{t_\mathrm{d}} \mathrm{d}t\,[\delta\hat{n}_1(\vec{x},t) - \delta\hat{n}_2(\vec{x},t+\Delta t)]$$
$$= \sum_{i,j}\int_{t_\mathrm{d}} \mathrm{d}t\,[\delta\hat{n}_1^{ij}(t) - \delta\hat{n}_2^{ij}(t+\Delta t)], \tag{A.6}$$

where we have introduced the operator $\delta\hat{n}^{ij}(t) = \int_{D_{ij}}\mathrm{d}\vec{x}\,\delta\hat{n}(\vec{x},t)$, which represents the fluctuations in the number flux for pixel $(i,j)$. Note that $\langle\delta\hat{N}\rangle = 0$ and that the statistics of $\delta\hat{n}^{ij}(t)$ over all pixels in analysis region $A$ give a measure of the spatial properties of the beam.

We first look at the numerator in equation (A.1), which can be rewritten as

$$\langle\Delta^2[(\hat{N}_{\mathrm{p}1} - \hat{N}_{\mathrm{p}2}) - (\hat{N}_{\mathrm{c}1} - \hat{N}_{\mathrm{c}2})]\rangle = \langle\Delta^2(\delta\hat{N}_\mathrm{p} - \delta\hat{N}_\mathrm{c})\rangle = \langle(\delta\hat{N}_\mathrm{p})^2\rangle + \langle(\delta\hat{N}_\mathrm{c})^2\rangle - 2\langle\delta\hat{N}_\mathrm{p}\delta\hat{N}_\mathrm{c}\rangle. \tag{A.7}$$

From equation (A.4) and taking into account equation (A.5), we can show that the first term on the right-hand side, $\langle(\delta\hat{N}_\mathrm{p})^2\rangle$, takes the form

$$\langle(\delta\hat{N}_\mathrm{p})^2\rangle = \sum_{i,j}\sum_{k,l}\int_{t_\mathrm{d}}\mathrm{d}t\int_{t_\mathrm{d}}\mathrm{d}t'\,[\langle\delta\hat{n}_{\mathrm{p}1}^{ij}(t)\delta\hat{n}_{\mathrm{p}1}^{kl}(t')\rangle + \langle\delta\hat{n}_{\mathrm{p}2}^{ij}(t+\Delta t)\delta\hat{n}_{\mathrm{p}2}^{kl}(t'+\Delta t)\rangle]. \tag{A.8}$$

In the limit in which the effective pixel area after binning the EMCCD pixels into 'super-pixels' is larger than the coherence area, the resulting super-pixels are not correlated, which means that

$$\langle\delta\hat{n}_\mathrm{p}^{ij}(t)\delta\hat{n}_\mathrm{p}^{kl}(t')\rangle = \delta_{i,k}\delta_{j,l}\langle\delta\hat{n}_\mathrm{p}^{ij}(t)\delta\hat{n}_\mathrm{p}^{ij}(t')\rangle = \frac{\delta_{i,k}\delta_{j,l}}{2\pi}\int_{-\infty}^{\infty}\mathrm{d}\Omega\,\mathrm{e}^{-\mathrm{i}\Omega\tau}S_\mathrm{p}^{ij}(\Omega), \tag{A.9}$$

where we have used the fact that for a stationary process the two time correlation function is equal to the Fourier transform of the power spectrum, $S_\mathrm{p}^{ij}(\Omega)$, with $\tau = t' - t$. Thus, through the use of equation (A.9) and the fact that for a stationary process the correlation function only depends on the time difference, equation (A.8) takes the form

$$\langle(\delta\hat{N}_\mathrm{p})^2\rangle = \frac{1}{\pi}\sum_{i,j}\int_{-\infty}^{\infty}\mathrm{d}\Omega\,S_\mathrm{p}^{ij}(\Omega)\int_{t_\mathrm{d}}\mathrm{d}t\int_{t_\mathrm{d}}\mathrm{d}t'\,\mathrm{e}^{-\mathrm{i}\Omega(t'-t)}. \tag{A.10}$$

Finally, in our experiments the effective integration time is determined by the temporal profile of the input probe pulse. As a result, for an intensity temporal profile $f(t)$ of the input probe, we can write equation (A.10) as

$$\langle(\delta\hat{N}_\mathrm{p})^2\rangle = \frac{1}{\pi}\sum_{i,j}\int_{-\infty}^{\infty}\mathrm{d}\Omega\,S_\mathrm{p}^{ij}(\Omega)\int_{-\infty}^{\infty}\mathrm{d}t\,f(t)\mathrm{e}^{\mathrm{i}\Omega t}\int_{-\infty}^{\infty}\mathrm{d}t'\,f(t')\,\mathrm{e}^{-\mathrm{i}\Omega t'}$$
$$= \frac{1}{\pi}\sum_{i,j}\int_{-\infty}^{\infty}\mathrm{d}\Omega|F(\Omega)|^2S_\mathrm{p}^{ij}(\Omega), \tag{A.11}$$

where $F(\Omega)$ is the Fourier transform of $f(t)$. As can be seen from this result, the spatial variance for the probe is given by the quadrature sum of the noise (power spectrum) over all pixels integrated over a frequency range determined by the magnitude squared of the Fourier transform of the intensity temporal profile of the input seed probe pulse. This is to be expected, as the super-pixels are uncorrelated in the limit of a binning area larger than the coherence area. Following a similar procedure for the other two terms of equation (A.7), we find that the numerator of equation (A.1) takes the form

$$\langle\Delta^2[(N_{\mathrm{p}1} - N_{\mathrm{p}2}) - (N_{\mathrm{c}1} - N_{\mathrm{c}2})]\rangle = \frac{1}{\pi}\sum_{i,j}\int_{-\infty}^{\infty}\mathrm{d}\Omega|F(\Omega)|^2[S_\mathrm{p}^{ij}(\Omega) + S_\mathrm{c}^{ij}(\Omega) - 2S_{\mathrm{p,c}}^{ij}(\Omega)], \tag{A.12}$$

where $S_\mathrm{c}^{ij}(\Omega)$ is the power spectrum for the conjugate and $S_{\mathrm{p,c}}^{ij}(\Omega)$ is the cross probe-conjugate power spectrum.

For the denominator, we can use as a starting point equation (A.12) and specialize to the case in which the probe and conjugate beams are replaced with coherent states of equal power and spatial profile. In this case the cross power spectrum vanishes as the two coherent states are uncorrelated and the denominator thus takes the form

$$\langle\Delta^2[(N_{\mathrm{p}1} - N_{\mathrm{p}2}) - (N_{\mathrm{c}1} - N_{\mathrm{c}2})]\rangle_{\mathrm{CS}} = \frac{1}{\pi}\sum_{i,j}(S_{\mathrm{SN,p}}^{ij} + S_{\mathrm{SN,c}}^{ij})\int_{-\infty}^{\infty}\mathrm{d}\Omega|F(\Omega)|^2, \tag{A.13}$$

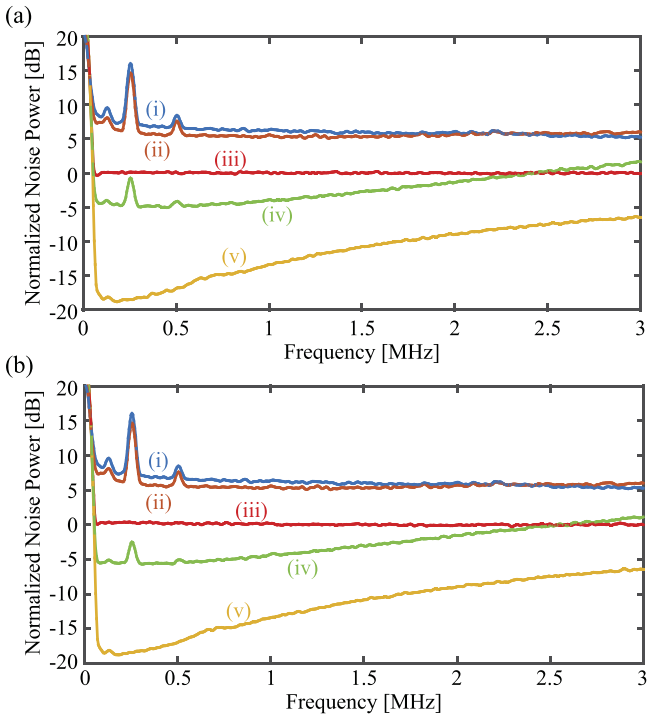


**Figure A1.** Normalized noise power spectra for the (a) near field and (b) far field configurations. The different traces represent the normalized noise spectra for the (i) probe, (ii) conjugate, and (iv) intensity difference. Trace (iii) gives the measured shot noise, which as expected is at 0 dB, and trace (v) represents the electronic noise of our detection system.

where we have used the fact that the shot noise is white noise (i.e. independent of frequency) and $S^{ij}_{\mathrm{SN,p}}$ ($S^{ij}_{\mathrm{SN,c}}$) is the shot noise level for the probe (conjugate) for pixel $(i, j)$. Finally, for simplicity we assume the mean value of the photocounts to be uniform over the detection area $A$, such that the shot noise power spectrum is the same for all pixels. Under this assumption we find that the denominator takes the form

$$\langle \Delta^2[(N_{\mathrm{p1}} - N_{\mathrm{p2}}) - (N_{\mathrm{c1}} - N_{\mathrm{c2}})]\rangle_{\mathrm{CS}} = \frac{M_x M_y}{\pi}(S_{\mathrm{SN,p}} + S_{\mathrm{SN,c}})\int_{-\infty}^{\infty} \mathrm{d}\Omega |F(\Omega)|^2, \tag{A.14}$$

where $M_x$ ($M_y$) is the number of pixels in the analysis region along the $x$ ($y$) direction.

From equations (A.12) and (A.14) we have that the NR takes the form

$$\begin{aligned}\mathrm{NR} &= \frac{1}{M_x M_y}\sum_{i,j}\int_{-\infty}^{\infty}\mathrm{d}\Omega\left(\frac{|F(\Omega)|^2}{\int_{-\infty}^{\infty}\mathrm{d}\Omega'|F(\Omega')|^2}\right)\left[\frac{S^{ij}_{\mathrm{p}}(\Omega) + S^{ij}_{\mathrm{c}}(\Omega) - 2S^{ij}_{\mathrm{p,c}}(\Omega)}{S_{\mathrm{SN,p}} + S_{\mathrm{SN,c}}}\right] \\ &= \frac{1}{M_x M_y}\sum_{i,j}\int_{-\infty}^{\infty}\mathrm{d}\Omega\, G(\Omega) S^{ij}_{\mathrm{diff}}(\Omega),\end{aligned} \tag{A.15}$$

where $S^{ij}_{\mathrm{diff}}(\Omega) \equiv [S^{ij}_{\mathrm{p}}(\Omega) + S^{ij}_{\mathrm{c}}(\Omega) - 2S^{ij}_{\mathrm{p,c}}(\Omega)]/[S_{\mathrm{SN,p}} + S_{\mathrm{SN,c}}]$ is the normalized intensity difference noise power spectrum and $G(\Omega) \equiv |F(\Omega)|^2/\int_{-\infty}^{\infty}\mathrm{d}\Omega|F(\Omega)|^2$ effectively acts as a normalized frequency filter that selects the portion of the squeezing spectrum to integrate over. As can be seen from this expression, spatial squeezing results from the presence of temporal squeezing in the twin beams. In fact, in the limit that the area covered by the binned pixels (super-pixel) is larger than the coherence area, the noise reduction factor NR will be equal to the average over all pixels of the normalized intensity difference noise spectra integrated over the frequency region determined by $G(\Omega)$.

For our experiment the normalized intensity difference noise power spectra for the near and far field configurations are shown in figures A1(a) and (b), respectively. For both configurations, we have measured the probe (trace i) and conjugate (trace ii) noise spectra, shot noise (trace iii), probe and conjugate intensity difference noise spectrum (trace iv), and electronic noise (trace v). All noise traces have been normalized to their corresponding shot noise. As can be seen from these figures, we have a maximum intensity difference squeezing of 5.07 dB and 5.75 dB in the near and far field configurations, respectively. While in principle we should expect the spatial squeezing to saturate at levels close to the maximum intensity difference squeezing as a function of binning, our measured degree of spatial squeezing saturates at 1 dB. This is most likely due

to a combination of the reduced quantum efficiency of the EMCCD (∼70%) with respect to the photodiodes used to measure the intensity difference squeezing (∼95%) and the fact that the two frame subtraction procedure that we implement is not able to cancel out all the low frequency classical technical noise present in the twin beams.

## ORCID iDs

Ashok Kumar https://orcid.org/0000-0001-6471-6946
Gaurav Nirala https://orcid.org/0000-0001-6216-7592
Alberto M Marino https://orcid.org/0000-0001-5377-1122

## References

[1] Horodecki R, Horodecki P, Horodecki M and Horodecki K 2009 Quantum entanglement *Rev. Mod. Phys.* **81** 865
[2] Nielsen M and Chuang I 2000 *Quantum Computation and Quantum Information* (Cambridge: Cambridge University Press)
[3] Bruss D and Leuchs G (ed) 2019 *Quantum Information: From Foundations to Quantum Technology Applications* (New York: Wiley)
[4] Bouwmeester D, Pan J-W, Mattle K, Eibl M, Weinfurter H and Zeilinger A 1997 Experimental quantum teleportation *Nature* **390** 575–9
[5] Karlsson A, Koashi M and Imoto N 1999 Quantum entanglement for secret sharing and secret splitting *Phys. Rev.* A **59** 162
[6] Huelga S F, Macchiavello C, Pellizzari T, Ekert A K, Plenio M B and Cirac J I 1997 Improvement of frequency standards with quantum entanglement *Phys. Rev. Lett.* **79** 3865
[7] Kimble H J 2008 The quantum internet *Nature* **453** 1023–30
[8] Giovannetti V, Lloyd S and Maccone L 2011 Advances in quantum metrology *Nat. Photon.* **5** 222–9
[9] Boyer V, Marino A M, Pooser R C and Lett P D 2008 Entangled images from four-wave mixing *Science* **321** 544–7
[10] Marino A M, Pooser R C, Boyer V and Lett P D 2009 Tunable delay of Einstein–Podolsky–Rosen entanglement *Nature* **457** 859–62
[11] The LIGO Scientific Collaboration 2011 A gravitational wave observatory operating beyond the quantum shot-noise limit *Nat. Phys.* **7** 962–5
[12] Dowran M, Kumar A, Lawrie B J, Pooser R C and Marino A M 2018 Quantum-enhanced plasmonic sensing *Optica* **5** 628–33
[13] Howell J C, Bennink R S, Bentley S J and Boyd R W 2004 Realization of the Einstein–Podolsky–Rosen paradox using momentum- and position-entangled photons from spontaneous parametric down conversion *Phys. Rev. Lett.* **92** 210403
[14] Edgar M P, Tasca D S, Izdebski F, Warburton R E, Leach J, Agnew M, Buller G S, Boyd R W and Padgett M J 2012 Imaging high-dimensional spatial entanglement with a camera *Nat. Commun.* **3** 984
[15] Moreau P-A, Mougin-Sisini J, Devaux F and Lantz E 2012 Realization of the purely spatial Einstein–Podolsky–Rosen paradox in full-field images of spontaneous parametric down-conversion *Phys. Rev.* A **86** 010101(R)
[16] Moreau P-A, Devaux F and Lantz E 2014 Einstein–Podolsky–Rosen paradox in twin images *Phys. Rev. Lett.* **113** 160401
[17] Lee J-C, Park K-K, Zhao T-M and Kim Y-H 2016 Einstein–Podolsky–Rosen entanglement of narrow-band photons from cold atoms *Phys. Rev. Lett.* **117** 250501
[18] Kumar A, Nunley H and Marino A M 2017 Observation of spatial quantum correlations in the macroscopic regime *Phys. Rev.* A **95** 053849
[19] Dabrowski M, Parniak M and Wasilewski W 2017 Einstein–Podolsky–Rosen paradox in a hybrid bipartite system *Optica* **4** 272–5
[20] Reichert M, Defienne H and Fleischer J W 2018 Massively parallel coincidence counting of high-dimensional entangled states *Sci. Rep.* **8** 7925
[21] Hordell J, Benedicto-Orenes D, Petrov P G, Kowalczyk A U, Barontini G and Boyer V 2018 Transport of spatial squeezing through an optical waveguide *Opt. Express* **26** 22783–92
[22] Bechmann-Pasquinucci H and Tittel W 2000 Quantum cryptography using larger alphabets *Phys. Rev.* A **61** 062308
[23] Wang C, Deng F-G, Li Y-S, Liu X-S and Long G L 2005 Quantum secure direct communication with high-dimension quantum superdense coding *Phys. Rev.* A **71** 044305
[24] Huber M and Pawłowski M 2013 Weak randomness in device-independent quantum key distribution and the advantage of using high-dimensional entanglement *Phys. Rev.* A **88** 032309
[25] Mirhosseini M, Magaña-Loaiza O S, O'Sullivan M N, Rodenburg B, Malik M, Lavery M P J, Padgett M J, Gauthier D J and Boyd R W 2015 High-dimensional quantum cryptography with twisted light *New J. Phys.* **17** 033033
[26] Krenn M, Huber M, Fickler R, Lapkiewicz R, Ramelow S and Zeilinger A 2014 Generation and confirmation of a (100 × 100)-dimensional entangled quantum system *Proc. Natl Acad. Sci.* **111** 6243
[27] Martin A, Guerreiro T, Tiranov A, Designolle S, Fröwis F, Brunner N, Huber M and Gisin N 2017 Quantifying photonic high-dimensional entanglement *Phys. Rev. Lett.* **118** 110501
[28] Pittman T B, Shih Y H, Strekalov D V and Sergienko A V 1995 Optical imaging by means of two-photon quantum entanglement *Phys. Rev.* A **52** R3429
[29] Kolobov M I 1999 The spatial behavior of nonclassical light *Rev. Mod. Phys.* **71** 1539
[30] Treps N, Grosse N, Bowen W P, Fabre C, Bachor H A and Lam P K 2003 A quantum laser pointer *Science* **301** 940–3
[31] Kolobov M I 2007 *Quantum Imaging* (New York: Springer)
[32] Brida G, Genovese M and Ruo Berchera I 2010 Experimental realization of sub-shot-noise quantum imaging *Nat. Photon.* **4** 227–30
[33] Walborn S P, Monken C H, Pádua S and Ribeiro P H S 2010 Spatial correlations in parametric down-conversion *Phys. Rep.* **495** 87–139
[34] Genovese M 2016 Real applications of quantum imaging *J. Opt.* **18** 073002
[35] Simon D S, Jaeger G and Sergienko A V 2017 *Quantum Metrology, Imaging, and Communication* (New York: Springer)
[36] Einstein A, Podolsky B and Rosen N 1935 Can quantum-mechanical description of physical reality be considered complete? *Phys. Rev.* **47** 777
[37] Bell J S 1964 On the Einstein Podolsky Rosen paradox *Physics* **1** 195

[38] Clauser J F, Horne M A, Shimony A and Holt R A 1969 Proposed experiment to test local hidden-variable theories *Phys. Rev. Lett.* **23** 880
[39] Aspect A, Grangier P and Roger G 1981 Experimental tests of realistic local theories via bell's theorem *Phys. Rev. Lett.* **47** 460
[40] Banaszek K and Wódkiewicz K 1998 Nonlocality of the Einstein–Podolsky–Rosen state in the Wigner representation *Phys. Rev.* A **58** 4345
[41] Fadel M, Zibold T, Décamps B and Treutlein P 2018 Spatial entanglement patterns and Einstein–Podolsky–Rosen steering in Bose–Einstein condensates *Science* **360** 409–13
[42] Kunkel P, Prüfer M, Strobel H, Linnemann D, Frölian A, Gasenzer T, Gärttner M and Oberthaler M K 2018 Spatially distributed multipartite entanglement enables EPR steering of atomic clouds *Science* **360** 413–6
[43] Lange K, Peise J, Lücke B, Kruse I, Vitagliano G, Apellaniz I, Kleinmann M, Tóth G and Klempt C 2018 Entanglement between two spatially separated atomic modes *Science* **360** 416–8
[44] Reid M D 1989 Demonstration of the Einstein–Podolsky–Rosen paradox using nondegenerate parametric amplification *Phys. Rev.* A **40** 913
[45] Reid M D, Drummond P D, Bowen W P, Cavalcanti E G, Lam P K, Bachor H A, Andersen U L and Leuchs G 2009 Coll.: the Einstein–Podolsky–Rosen paradox: from concepts to applications *Rev. Mod. Phys.* **81** 1727
[46] Taylor M A, Janousek J, Daria V, Knittel J, Hage B, Bachor H-A and Bowen W P 2013 Biological measurement beyond the quantum limit *Nat. Photon.* **7** 229–33
[47] Andrews M R, Mewes M-O, van Druten N J, Durfee D S, Kurn D M and Ketterle W 1996 Direct, nondestructive observation of a Bose condensate *Science* **273** 84–7
[48] WilsonK E, Newman Z L, Lowney J D and Anderson B P 2015 *In situ* imaging of vortices in Bose–Einstein condensates *Phys. Rev.* A **91** 023621
[49] Nogrette F, Labuhn H, Ravets S, Barredo D, Bóguin L, Vernier A, Lahaye T and Browaeys A 2014 Single-atom trapping in holographic 2D arrays of microtraps with arbitrary geometries *Phys. Rev.* X **4** 021034
[50] Duan L-M, Giedke G, Cirac J I and Zoller P 2000 Inseparability criterion for continuous variable systems *Phys. Rev. Lett.* **84** 2722
[51] Agafonov I N, Chekhova M V and Leuchs G 2010 Two-color bright squeezed vacuum *Phys. Rev.* A **82** 011801(R)
[52] Chekhova M V, Leuchs G and Żukowski M 2015 Bright squeezed vacuum: entanglement of macroscopic light beams *Opt. Commun.* **337** 27–43
[53] Martinelli M, Treps N, Ducci S, Gigan S, Maître A and Fabre C 2003 Experimental study of the spatial distribution of quantum correlations in a confocal optical parametric oscillator *Phys. Rev.* A **67** 023808
[54] Kumar A and Marino A M 2019 Spatial squeezing in bright twin beams generated with four-wave mixing: constraints on characterization with an electron-multiplying charge-coupled-device camera *Phys. Rev.* A **100** 063828
[55] Kumar A, Nunley H and Marino A M 2018 Comparison of coherence-area measurement techniques for bright entangled twin beams *Phys. Rev.* A **98** 043853
[56] Ndagano B, Defienne H, Lyons A, Starshynov I, Villa F, Tisa S and Faccio D 2020 Imaging and certifying high-dimensional entanglement with a single-photon avalanche diode camera *Npj Quantum Inf.* **6** 94
[57] Lantz E, Denis S, Moreau P-A and Devaux F 2015 Einstein–Podolsky–Rosen paradox in single pairs of images *Opt. Express* **23** 26472–8
[58] Hammerer K, Sørensen A S and Polzik E S 2010 Quantum interface between light and atomic ensembles *Rev. Mod. Phys.* **82** 1041